Available online at www.sciencedirect.com
ScienceDirect
Combustion and Flame 154 (2008) 319–330
Combustion and Flame
www.elsevier.com/locate/combustflame

Counterflow diffusion flames of general fluids: Oxygen/hydrogen mixtures

Guillaume Ribert [a,*], Nan Zong [a], Vigor Yang [a], Laetitia Pons [b], Nasser Darabiha [b], Sébastien Candel [b]

[a] *Department of Mechanical and Nuclear Engineering, The Pennsylvania State University, University Park, PA 16802, USA*
[b] *Laboratoire EM2C, CNRS and Ecole Centrale Paris, 92295 Châtenay-Malabry, France*

Received 12 February 2007; received in revised form 18 February 2008; accepted 29 April 2008

Available online 12 June 2008

Abstract

A comprehensive framework has been established for studying laminar counterflow diffusion flames for general fluids over the entire regime of thermodynamic states. The model incorporates a unified treatment of fundamental thermodynamic and transport theories into an existing flow solver DMCF to treat detailed chemical kinetic mechanisms and multispecies transport. The resultant scheme can thus be applied to fluids in any state. Both subcritical and supercritical conditions are considered. As a specific example, diluted and undiluted H_2/O_2 flames are investigated at pressures of 1–25 MPa and oxygen inlet temperatures of 100 and 300 K. The effects of pressure p and strain rate ϵ_s on the heat release rate $\dot{q}_s$, extinction limit, and flame structure are examined. In addition, the impact of cross-diffusion terms, such as the Soret and Dufour effects, on the flame behavior is assessed. Results indicate that the flame thickness δ_f and heat release rate correlate well with the square root of the pressure multiplied by the strain rate as $\delta_f \sim 1/\sqrt{p\epsilon_s}$ and $\dot{q}_s \sim \sqrt{p\epsilon_s}$, respectively. The strain rate at the extinction limit exhibits a quasi-linear dependence on p. Significant real-fluid effects take place in the transcritical regimes, as evidenced by the steep property variations in the local flowfield. However, their net influence on the flame properties appears to be limited due to the ideal-gas behavior of fluids in the high-temperature zone.

Keywords: Counterflow diffusion flames; Real fluids; Effects of pressure and strain rate; Transcritical; Supercritical states

1. Introduction

Laminar counterflow diffusion flames provide much useful information about the basic properties of nonpremixed combustion. Several numerical codes incorporating detailed chemical kinetic mechanisms and multispecies transport, such as the Detailed Modeling of Counterflow Flame (DMCF) code [1,2], have been developed to study flame behavior under various flow conditions. For instance, the effects of strain rate on burning behavior and flame stability were examined systematically for a variety of fuel/oxidizer combinations [3]. Results have been applied as a submodel in numerical calculations of turbulent diffusion flames in the flamelet regime, in which the flame is locally assumed to bear a laminar structure. Thus, a thorough understanding of strained laminar flames

* Corresponding author.
E-mail address: ribert@coria.fr (G. Ribert).

0010-2180/$ – see front matter
doi:10.1016/j.combustflame.2008.04.023

is a prerequisite to achieving improved knowledge of more complex systems.

Most existing studies of counterflow diffusion flames have been carried out at low and moderate pressures. The effects of supercritical conditions, which often occur in high-pressure combustion devices [4], are less well documented. Most of the previous studies have dealt with systems involving either a gaseous or a liquid-spray fuel against an air flow. The influence of strain rate, inlet temperature, and radiative heat losses on flame structures was numerically investigated and compared with experimental data. Sung et al. [5] have shown both experimentally and numerically that the flame thickness varies inversely with the square root of the strain rate (ϵ_s) for a methane/oxygen/nitrogen diffusion flame at 1 atm. Brown et al. [6] studied effects of hydrogen dilution by nitrogen for diffusion flames involving an 80/20 H_2/N_2 mixture and air. Good agreement was obtained between the numerical and experimental results. The flame thickness, taken to be the full width at half maximum of the measured H_2O profiles, also varied with $1/\sqrt{\epsilon_s}$. Balakrishnan et al. [7] examined the extinction and ignition limits for diluted and undiluted H_2/O_2 diffusion flames in the pressure range 0.25–10 bar using both full and reduced chemical kinetic schemes. The critical strain rate at extinction was found to increase rapidly with increasing pressure. Williams [8] examined the effects of transport on nonpremixed flame structures and extinction characteristics and observed that the strain rate corresponding to the extinction limit is sensitive to molecular transport. A related study was later carried out numerically by Ben Dakhlia et al. [9] on diffusion flames involving n-heptane/O_2/N_2. The Soret effect was found to be dependent on the diluent considered (i.e., nitrogen or helium) and appeared in the flame structure and fuel–vapor diffusion boundary layer. Juniper et al. [10] considered the counterflow diffusion flames formed by gaseous hydrogen impinging on a pool of liquid oxygen and gaseous hydrogen at 1 and 2 bar using a perfect-gas law. The oxygen temperature was set to 90 K, whereas the hydrogen temperature varied from 20 to 310 K. Results indicated that the heat-release rate per unit surface area is proportional to the square root of the pressure multiplied by the strain rate. It was also found that the strain rate at the extinction limit increases with pressure, a phenomenon consistent with the experimental results for n-heptane/air flames [11]. Schlotz and Gutheil [12] studied laminar spray counterflow flames for liquid-fuel-rocket applications. Liquid oxygen diluted with gaseous hydrogen was injected against a hydrogen stream. A subcritical pressure of $p = 30$ bar was considered along with cryogenic inlet temperatures (gas at 100 K and liquid at 80 K). The flame structure revealed two temperature peaks, one near the spray injection location due to vaporization and the other close to the stagnation point corresponding to the diffusion flame front. The flame was found to be very sensitive to the equivalence ratio and strain rate.

The present work deals with effects of pressure on laminar counterflow diffusion flames. Emphasis is placed on the supercritical conditions typically encountered in high-pressure combustion devices such liquid-propellant rockets, and diesel and gas-turbine engines. A notable example is provided by the thrust chamber of the Vulcain 2 engine [13], in which liquid oxygen (LOx) is injected at a subcritical temperature of 80 K into a high-pressure environment of 11.5 MPa. The condition can be compared with the thermodynamic critical temperature and pressure of oxygen, which are 154.8 K and 5.04 MPa, respectively. Under this situation, the injected LOx heats up rapidly and its interface with the surrounding gases prevails over a short distance from the injection plane. The dense core disappears progressively as mass is transferred from the core to the surroundings. Several experimental [14–17] and numerical [18–20] studies have been carried out to characterize the supercritical flame structures of shear co-axial injectors fed by hydrogen and methane fuels. Detailed flow development and flame stabilization and spreading mechanisms were investigated in the near field of the injector exit.

Significant real-fluid effects featuring steep property variations take place when the fluid transits through the thermodynamic transcritical regime [4,21,22]. In contrast, the fluid behaves like an ideal gas in the high-temperature reaction and product zones. Palle et al. [23] conducted numerical simulations for unsteady one-dimensional laminar diffusion flames at a pressure of 10 MPa for N_2/O_2, $N_2/C_{12}H_{26}$, and H_2/O_2 mixtures. Three different models of a one-step reaction in the form $A + r_1C \rightarrow P$ were considered, and cross-diffusion terms were included. The Soret effect was found to be nonnegligible for species with disparate molecular weights, especially for the $H_2 + 1/2O_2 \rightarrow H_2O$ reaction. The Dufour effect was insignificant for all cases. Sohn et al. [24] studied numerically the structures and acoustic responses of undiluted H_2/O_2 diffusion flames at pressures up to 10 MPa. Both detailed and reduced chemical kinetic schemes were employed. The calculated strain rate at the extinction limit showed a quasi-linear pressure dependence. This result, obtained with a four-step reaction mechanism, remains to be checked with a more complete kinetic scheme.

The purpose of the present study is to develop a comprehensive numerical model capable of treating counterflow diffusion flames over the entire range of fluid thermodynamic states. Both subcritical and su-

Table 1
Survey of one-dimensional numerical studies of counterflow diffusion flames

Ref.	Red. χ	Det. χ	Rad.	$p < p_c$	$p > p_c$	Soret	Spary	ϵ_s	T	Fuel	Meas.	Misc.
[2]		X		X				X		H_2		Dilution, $\epsilon_s(t)$
[5]		X		X				X		CH_4	X	Unsteady
[6]		X		X				X		H_2	X	Dilution
[7]	X	X		X		X		X	X	H_2		Dilution
[9]		X		X		X	X			C_7H_{16}, CH_3OH		–
[10]		X		X				X	X	H_2		vs liquid O_2
[12]		X		X		X	X	X		H_2		vs liquid O_2
[23]	X				X	X				H_2, $C_{12}H_{26}$		Unsteady
[24]	X	X		X	X			X		H_2		Unsteady
[37]		X		X				X		H_2	X	Dilution, pressure effect
[38]		X		X		X		X		H_2		Part. premixed
[44]		X	X	X		X		X		H_2	X	–
[47]		X		X		X				H_2, CH_4		Dilution
Present study		X		X	X	X		X	X	H_2		–

Note. Red. χ and Det. χ stand for reduced and detailed chemistry, respectively, Rad. for radiation. Meas. stands for calculations compared with experimental data and Misc. stands for miscellaneous. ϵ_s and T represent variable strain rate and inlet temperature studies, respectively.

percritical conditions are examined. Such a general-fluid approach not only will allow us to explore the flame behavior under various fluid states, but also will serve as a fundamental tool for establishing flame submodels for treating turbulent combustion over a wide range of pressures. To this end, a detailed combustion modeling tool (DMCF) is first extended by implementing general-fluid thermodynamic theories [25], formulated in a unified manner. A general balance of energy is then derived, and thermophysical properties are evaluated with a self-consistent scheme valid for general fluids [4]. As a specific example, the present analysis is employed to investigate H_2/O_2 and H_2/air diffusion flames in both subcritical and supercritical environments. The influences of pressure and strain rate on the flame structure and heat release rate are examined systematically. In addition, the Soret and Dufour effects are incorporated for light species based on formulas developed for ideal gases [26]. The work appears to be the most complete of its kind to date in the study of laminar counterflow diffusion flames, as indicated in Table 1, which summarizes various existing studies in the subject area.

2. Theoretical formulation

The physical model considered here is an axisymmetric laminar diffusion flame stabilized near the stagnation plane of two opposing streams, as shown schematically in Fig. 1. The theoretical basis for treating such a flame configuration is well established for perfect gases [2,27,28]. A constant strain rate, ϵ_s, defined as the radial gradient of the radial velocity, $\partial u/\partial x$, at the fuel boundary is assumed. Following the approach of Meng and Yang [25], the analysis

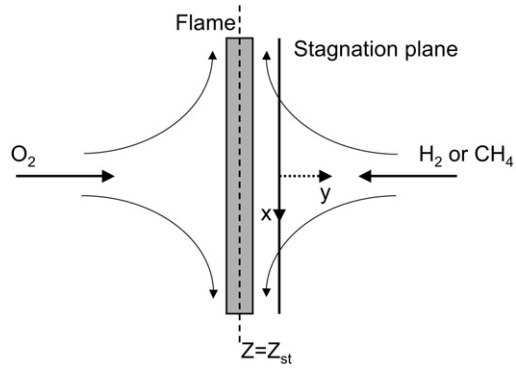

Fig. 1. Schematic view of a counterflow diffusion flame.

is extended by incorporating general-fluid thermodynamics theories and property evaluation schemes, so that the flame behavior over the entire regime of fluid states can be formulated in a unified manner.

2.1. Governing equations

Near the axis of symmetry, the balance equations of mass, momentum, species mass fractions, and enthalpy for a counterflow flame with a fixed strain rate can be expressed in the forms

- Mass

$$\frac{\partial \rho}{\partial t} = -\frac{\partial \rho v}{\partial y} - 2\rho\epsilon_s u^+; \tag{1}$$

- Radial momentum

$$\rho\frac{\partial u^+}{\partial t} = \frac{\partial}{\partial y}\left(\mu\frac{\partial u^+}{\partial y}\right) - \rho v\frac{\partial u^+}{\partial y} + \epsilon_s\left(\rho_{+\infty} - \rho u^{+2}\right); \tag{2}$$

- Species concentration

$$\rho\frac{\partial Y_k}{\partial t} = -\rho v\frac{\partial Y_k}{\partial y} - \frac{\partial}{\partial y}(\rho Y_k V_k) + W_k\dot{\omega}_k, \quad k = 1,\ldots,N_s; \tag{3}$$

- Energy

$$\rho c_p\frac{DT}{Dt} = \frac{\partial}{\partial y}\left(\lambda\frac{\partial T}{\partial y}\right) - \left(\rho\sum_{k=1}^{N_s} Y_k V_k\frac{\partial \bar{h}_k}{\partial y}\right) - \sum_{k=1}^{N_s}\bar{h}_k W_k\dot{\omega}_k, \tag{4}$$

where ρ is the density, Y_k, V_k, W_k, and $\dot{\omega}_k$ the mass fraction, diffusion velocity, molecular weight, and reaction rate of species k, respectively, $u^+ = u/\epsilon_s x$ the reduced radial velocity, v the axial velocity, and μ the viscosity. The partial-mass enthalpy of species k, $\bar{h}_k$, is introduced to account for the interactions between molecules of different components in a general-fluid mixture [25]. It is defined by the total mass of the mixture, m, and the partial masses of all constituent components, m_k:

$$\bar{h}_k = \left(\frac{\partial mh}{\partial m_k}\right)_{T,p,m_{k\neq l}}. \tag{5}$$

The specific enthalpy of the mixture, h, thus becomes

$$h = \sum_{k=1}^{N_s} Y_k\bar{h}_k. \tag{6}$$

2.2. Thermodynamic properties and equation of state (EOS)

Thermodynamic properties, such as internal energy, enthalpy, and constant-pressure specific heat, are evaluated based on fundamental thermodynamic theories. Each property can be conveniently expressed as the sum of the ideal-gas counterpart at the same temperature and a departure function that accounts for the dense-fluid correction. Thus,

$$e(T,\rho) = e_0(T) + \int_{\rho_0}^{\rho}\left[\frac{p}{\rho^2} - \frac{T}{\rho^2}\left(\frac{\partial p}{\partial T}\right)_\rho\right]_T d\rho, \tag{7}$$

$$h(T,\rho) = h_0(T) + \int_{p_0}^{p}\left[\frac{1}{\rho} - \frac{T}{\rho^2}\left(\frac{\partial \rho}{\partial T}\right)_p\right]_T dp, \tag{8}$$

$$C_p(T,\rho) = C_{v_0}(T) - \int_{\rho_0}^{\rho}\left[\frac{T}{\rho^2}\left(\frac{\partial^2 p}{\partial T^2}\right)_\rho\right]_T d\rho + \frac{T}{\rho^2}\left(\frac{\partial^2 p}{\partial T^2}\right)_\rho \Big/ \left(\frac{\partial p}{\partial \rho}\right)_T, \tag{9}$$

where the subscript 0 refers to the ideal state at low pressure. The departure functions on the right-hand sides of Eqs. (7)–(9) are determined using an appropriate equation of state. In the present study, a modified Soave–Redlich–Kwong (SRK) equation of state [29,30] is chosen due to its ease of implementation and wide range of validity in modeling the fluid p–V–T behavior, except in proximity to the critical point [31].

This equation takes the form

$$p = \frac{\rho RT}{(W - b\rho)} - \frac{a\alpha}{W}\frac{\rho^2}{(W + b\rho)}, \tag{10}$$

where R is the universal gas constant and W the molecular weight of the fluid mixture. The two parameters, a and b, taking into account the effects of attractive and repulsive forces among molecules, respectively, are calculated with the mixing rules

$$a\alpha = \sum_{i=1}^{N_s}\sum_{j=1}^{N_s} X_i X_j\alpha_{ij}a_{ij}, \tag{11}$$

$$\alpha_{ij}a_{ij} = \sum_{i=1}^{N_s}\sum_{j=1}^{N_s}\sqrt{\alpha_i\alpha_j a_i a_j}(1-\kappa_{ij}), \tag{12}$$

$$b = \sum_{i=1}^{N_s} X_i b_i, \tag{13}$$

where X_k is the mole fraction of species k and κ_{ij} the binary interaction coefficient [30]. The constants a_i and b_i are determined from the universal relationships

$$a_i = 0.42747\frac{R^2T_{c_k}^2}{p_{c_k}} \quad \text{and} \quad b_i = 0.08664\frac{RT_{c_k}}{p_{c_k}}, \tag{14}$$

where T_{c_k} and p_{c_k} represent the critical temperature and pressure of species k, respectively. The third parameter, α_i, is given by

$$\alpha_i = \left[1 + S_i\left(1 - \sqrt{\frac{T}{T_{c_k}}}\right)\right]^2, \tag{15}$$

where S_i is a function of the acentric factor, ω_i:

$$S_i = 0.48508 + 1.5517\omega_i - 0.15613\omega_i^2. \tag{16}$$

2.3. Transport properties

Accurate evaluation of transport properties is crucial for the study of high-pressure flow and flame dynamics. To account for the continuous variation of fluid properties in a supercritical environment, one cannot use classical techniques that deal individually with liquids or gases. In the present study, both the

mixture viscosity, μ, and the thermal conductivity, λ, are determined by the method proposed by Chung et al. [32], which extends the Chapman–Enskog theory by introducing a dense-fluid correction. The calculated properties agree well with the NIST experimental data for both the gas and liquid phases [33]. Estimation of the binary mass diffusivity for a fluid mixture at high pressures is a challenging task, due to the lack of a formal theory or even a theoretically based correlation. Takahashi [34] suggested a simple scheme for predicting the binary mass diffusivity of a dense fluid by means of a corresponding-state principle. The method, which was established based on curve fits of experimental data of various species over a wide range of pressures and temperatures, provides a relatively accurate estimate of the diffusion coefficient of a fluid mixture when the temperature is greater than the critical value. Model uncertainties, however, may arise when the reduced temperature of the mixture is smaller than unity because most of the data employed to validate the correlation belong to the near- or supercritical temperature regime.

2.4. Boundary conditions and numerical method

For a given fuel/oxidizer combination and flow condition, the flame structure is defined by the boundary conditions

$$T_{y\to-\infty} = T_{-\infty}, \qquad Y_{k,y\to-\infty} = Y_k^{-\infty},$$
$$u^+_{y\to-\infty} = \left(\frac{\rho_{+\infty}}{\rho_{-\infty}}\right)^{1/2}, \tag{17}$$
$$T_{y\to+\infty} = T_{+\infty}, \qquad Y_{k,y\to+\infty} = Y_k^{+\infty},$$
$$u^+_{y\to+\infty} = 1, \tag{18}$$

along with the additional relation $v_{y=0} = 0$.

The overall system of Eqs. (1)–(4) can be conveniently combined into the form

$$\frac{\partial \Psi}{\partial t} + \mathcal{F}(\Psi) = 0, \tag{19}$$

where Ψ is the solution vector and $\mathcal{F}$ is a differential operator. At steady state, this system becomes $\mathcal{F}(\Psi) = 0$. Equations (20) and the associated boundary conditions can be solved by means of a combination of time-marching and Newton iteration techniques [2]. A global adaptive grid is employed to refine the spatial resolution in regions with steep gradients.

3. Discussion of results

The theoretical and numerical framework outlined above has been employed to study H_2/O_2 counterflow diffusion flames under a variety of flow conditions. The work consists of two parts. First, the SRK EOS thermophysical property evaluation schemes are incorporated into the DMCF code, which is then validated over a wide range of subcritical pressures. The impact of the Soret and Dufour effects is also examined. Second, the flame behavior under transcritical and supercritical conditions is explored. Emphasis is placed on the influence of pressure and strain rate on the flame properties and heat release distributions.

3.1. Subcritical pressures

The H_2/O_2 reaction mechanism employed in the present study was developed by Li et al. [35]. The scheme is extended from the work of Muller et al. [36] and contains eight reacting species (H_2, O_2, H, O, OH, HO_2, H_2O, and H_2O_2) and 19 reversible reactions. Validated for a wide range of experimental conditions ($T \in [298–3000\ \text{K}]$, $p \in [0.25–87\ \text{bar}]$) for laminar premixed flames in shock tubes and flow reactors, the mechanism has been implemented with success in simulating nonpremixed H_2/air counterflow flames [37,38].

Three different approaches are employed here to study the flame behavior at subcritical pressures:

(i) Designated as DMCF Ideal Gas: thermodynamic properties are determined from the CHEMKIN library [39] and transport properties from the TRANSPORT library [26], both for ideal gases.
(ii) Designated as DMCF-PRF (Partial Real Fluid): thermodynamic properties are determined based on the SRK EOS [25], whereas transport properties are estimated using the TRANSPORT library [26].
(iii) Designated as DMCF-RF (Real Fluid): thermodynamic properties are determined based on the SRK EOS [25], whereas transport properties are estimated using the techniques described in Section 2.3.

Fig. 2 shows the calculated temperature distributions under the standard conditions (i.e., $T_{H_2} = T_{O_2} = 300$ K, $p = 1$ bar). The strain rate is set to 20 s^{-1}. The ideal-gas (i) and real-fluid (iii) approaches lead to results close to each other. The flame thickness δ_f, defined as the full width at half maximum, is 22.5 mm for case (i) and 22 mm for case (iii). The temperature reaches maximum values of 3050 K for case (i) and 3075 K for case (iii), respectively, which both are close to the adiabatic flame temperature of $T_{ad} = 3080$ K for the stoichiometric H_2/O_2 mixture. The PRF simulation provides a higher maximum temperature and a thinner flame thickness. It should not even be used for flame simulations at atmospheric condi-

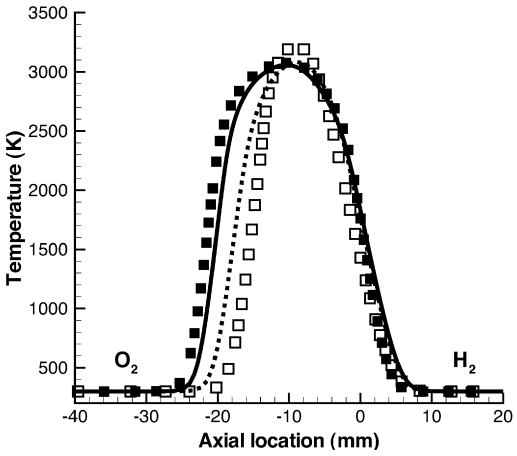

Fig. 2. Temperature profiles at $p = 1$ bar, $T_{O_2} = T_{H_2} = 300$ K, and $\epsilon_s = 20\ s^{-1}$. Case (i) is based on the ideal gas assumption [2] with $Le_k = 1$ (···) and $Le_k \neq 1$ (—); case (ii) only incorporates the SRK EOS (□); case (iii) incorporates the SRK EOS and general-fluid thermodynamics theories (■).

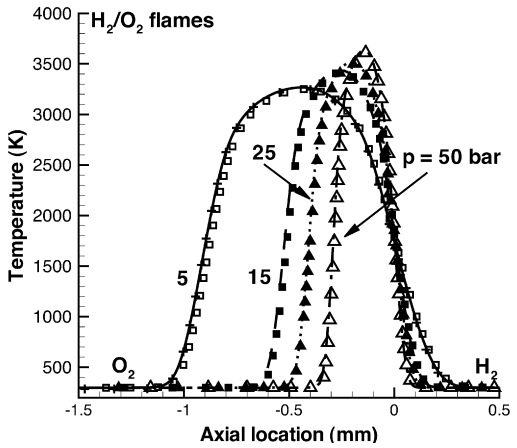

Fig. 3. Pressure effect on H_2/O_2 subcritical counterflow diffusion flames at $\epsilon_s = 2000\ s^{-1}$: lines (—, – –, and ···) correspond to diffusion velocities based on mole gradient, symbols (■, ▲, □, and △) include the Soret effect, and (+) represents the Dufour effect ($p = 5$ bar).

tions. The real fluid thermodynamics implemented in the present study (case (iii)) is thus validated in the ideal-gas limit.

Two other detailed chemical kinetic schemes were also tested for simulating the flame structure: the mechanism of Miller et al. [40] and the submechanism of Katta and Roquemore [41]. Almost identical results were obtained, except that the latter predicts a flame temperature near 4400 K. Accordingly, only the mechanism of Li et al. [35] is used in what follows.

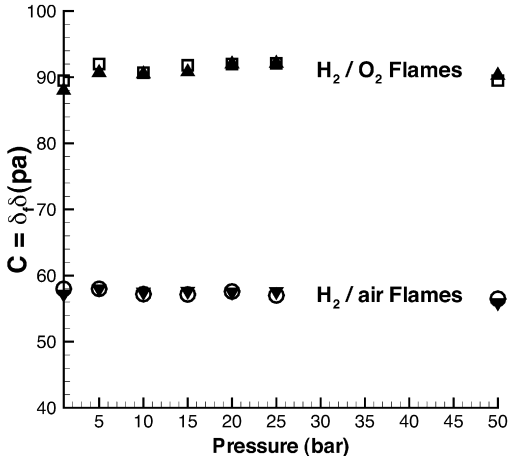

Fig. 4. Flame thickness parameter ($C = \delta_f\sqrt{p\epsilon_s}$), as a function of pressure p for H_2/air and H_2/O_2 counterflow diffusion flames at two different strain rates: (▲, ▼) for $\epsilon_s = 2000\ s^{-1}$ and (○, □) for $\epsilon_s = 8000\ s^{-1}$.

Fig. 3 shows the temperature profiles for different pressures at a fixed strain rate of 2000 s^{-1} for H_2/O_2 flames. According to the principle of Le Châtelier [42], a pressure increase in a combustion system reduces the amount of dissociation, and the maximum flame temperature increases. The flame thickness, however, exhibits an opposite trend. This can be explained through an asymptotic analysis [10]. The heat release per unit surface area is proportional to $\sqrt{p\epsilon_s}$, but the thermal conductivity remains basically pressure-independent. The reduction in flame thickness with pressure was also found by Law [43], who suggested the use of the pressure-weighted strain rate $p\epsilon_s$ in correlating the pressure effects. The flame thickness is thus proportional to $1/\sqrt{p\epsilon_s}$ (instead of $1/\sqrt{\epsilon_s}$), as shown in Fig. 4.

The Soret and Dufour effects are considered for light species [26]. With the Hirschfelder–Curtiss approximation for thermal diffusion (i.e., the Soret effect), the mass diffusion velocity can be expressed in the general form [26]

$$V_k = V_k^* + W_k^* + V_c = -D_k^* \frac{1}{X_k}\frac{\partial X_k}{\partial y} - \frac{D_k^*\theta_k^*}{X_k}\frac{1}{T}\frac{\partial T}{\partial y} + V_c, \tag{20}$$

where θ_k^* is the thermal-diffusion ratio [26], and

$$D_k^* = \frac{1 - Y_k}{\sum_{m\neq k} X_m/D_{km}}. \tag{21}$$

The correction velocity can be evaluated by the TRANSPORT package [26]:

$$V_c = -\sum_{k=1}^{N_s} Y_k\left(V_k^* + W_k^*\right). \tag{22}$$

Table 2
Critical pressure p_c and temperature T_c for species involved in the H_2/O_2 chemical mechanism

	H_2	O_2	H	O	OH	HO_2	H_2O	H_2O_2
p_c (bar)	13	50.4	88.2	76	85.4	82.8	221.2	93.5
T_c (K)	33.2	154.6	404.3	367.4	443.7	487.3	647.3	544.3

This approximation has been validated by Daguse et al. [44] against a complete kinetic theory for a counterflow $H_2/O_2/N_2$ diffusion flame at the atmospheric pressure. Results show that the two approaches are in good agreement. The calculated species and temperature profiles differ by 1% in location and the flame front is slightly displaced. The present method does not introduce significant error.

The impact of the Soret effect is shown by the solid symbols in Fig. 3. As a result of thermal diffusion, light molecules are driven toward hot gases and heavy molecules move in the opposite direction, thereby leading to a moderate change in the flame structure. Since hydrogen rapidly reacts with other species, thermal diffusion plays a slightly more important role on the oxidizer side, especially near the flame center, where light species are present. The inclusion of thermal diffusion thus results in a slight decrease in the flame thickness and temperature on the oxidizer side. This finding is consistent with the general observations in previous works. It should be noted that the present treatment of the Soret effect is based on an ideal-gas assumption. A more complete formulation, such as those described in [45,46], may be incorporated to include the pressure effect on thermal diffusion.

The impact of the Dufour effect, which accounts for the thermal diffusion induced by a concentration gradient (q_D), is examined by incorporating the following term into the enthalpy Eq. (4):

$$q_D = -p \sum_{k=1}^{N_s} \left(D_k^* \theta_k^* \frac{\partial X_k}{\partial y} \right). \tag{23}$$

The influence on the flame structure appears to be negligible, as evidenced in Fig. 3. The same conclusion was reached by Ern and Giovangigli [47] in their study on H_2/air and CH_4/air flames.

3.2. Supercritical pressures

The flame behavior in the supercritical-pressure regime of oxygen ($p > 5.04$ MPa) was investigated by means of the general framework described in Section 2. All the thermodynamic and transport properties are calculated using the real-fluid approach along with the SRK equation of state. The overall treatment is designated as DMCF-RF (full real-fluid). The chemical reaction mechanism is based on the detailed scheme proposed by Li et al. [35], which has been validated up to 87 atm in shock tubes. Nevertheless, further validation need to be conducted for the supercritical regime, for which the rate constants for bimolecular and termolecular reactions may be corrected as proposed by Schmitt et al. in [48].

Table 2 lists the critical pressures and temperatures of the species included in the reaction scheme. All the species except hydrogen have critical pressures and temperatures higher than those of oxygen, and thus may undergo thermodynamic phase transition to the liquid phase in regions away from the flame zone, depending on local flow conditions. This phenomenon, however, is not taken into account in the present analysis, because only small amounts of these species are present in the low-temperature regions where fluid condensation may occur.

Figs. 5a and 5b show the mass fractions of major and minor species at 50 and 100 bar. The inlet temperature is fixed at 300 K for both hydrogen and oxygen, and the strain rate is set to 2000 s^{-1}. As the pressure increases from 50 to 100 bar, the water vapor mass fraction remains the same in the flame zone, whereas the flame thickness varies inversely with $\sqrt{p}$. Since the diffusive transport (ρD) is pressure-insensitive, the intensity of chemical reactions becomes the dominant parameter of the combustion phenomenon [43]. Thus, considering a common reference position ($y = 0$ in Fig. 5) based on the H_2 profiles for all simulations, a pressure increase yields a shift of the species mass fractions toward the hydrogen side. The situation is, however, quite different for minor species. At a higher pressure, the H mass fraction decreases, and the relatively inactive HO_2 species increases through the $H + O_2 + M \rightarrow HO_2 + M$ reaction pathway. A small amount of H_2O_2 is produced through the HO_2–H_2O_2 chain mechanism. Fig. 6 shows the results for the oxygen inlet temperature of 100 K, with all the other conditions identical to those in Fig. 5. Only slight changes appear on the oxygen side, where a greater quantity of energy is needed to heat up and then react with oxygen. As a consequence, all species profiles are shifted toward the hydrogen side. The real-fluid effects play a role through species transport, inducing a small increase in the maximum of the intermediate species as compared with those shown in Fig. 5.

The distributions of the fluid density and thermophysical properties, including the compressibility fac-

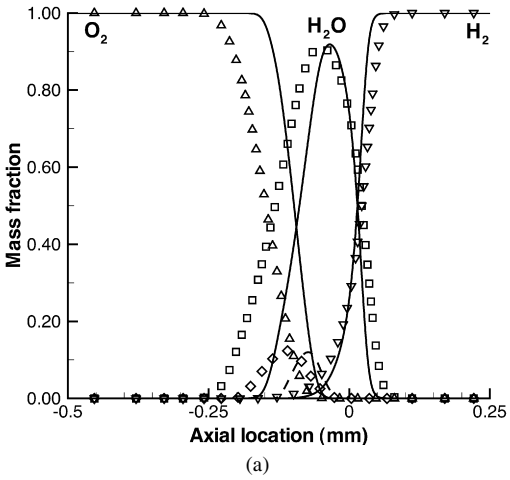

Fig. 5. Distributions of mass fractions of H_2/O_2 flames at 50 bar (lines) and 100 bar (symbols). $T_{H_2} = T_{O_2} = 300$ K and $\epsilon_s = 2000\ s^{-1}$; (a) major species profiles: O_2 (–·–, △), H_2 (···, ▽), H_2O (—, ■) and OH (––, ◆); (b) radical profiles: H (—, □), HO_2 (–·–, ◇), and H_2O_2 (···, ▽).

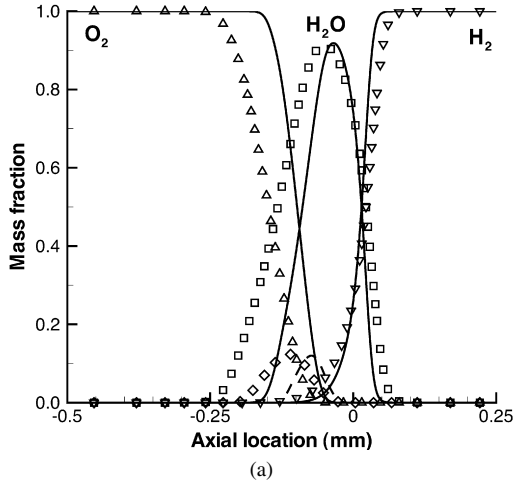

Fig. 6. Distributions of mass fractions of H_2/O_2 flames at 50 bar (lines) and 100 bar (symbols). $T_{H_2} = 300$ K, $T_{O_2} = 100$ K, and $\epsilon_s = 2000\ s^{-1}$; (a) major species profiles: O_2 (–·–, △), H_2 (···, ▽), H_2O (—, ■) and OH (––, ◆); (b) radical profiles: H (—, □), HO_2 (–·–, ◇), and H_2O_2 (···, ▽).

tor (Z), the Schmidt and Prandtl numbers ($Sc(k) = \mu/(\rho D_k^*)$ and $Pr = (\mu C_p)/\lambda$, respectively), and the specific heat, were obtained to explore their effects on the flame structure. These quantities are displayed in Figs. 7 and 8 for oxygen inlet temperatures of $T_{O_2} = 300$ and 100 K, respectively. The hydrogen temperature is fixed at 300 K, and the strain rate at 2000 s^{-1}. The condition of 50 bar is close to the critical pressure of oxygen and was chosen to permit an investigation of the effects on flame behavior of rapid property variations in the transcritical regime. In the case shown in Fig. 7, both the oxygen and hydrogen temperatures are supercritical. The compressibility factor is around unity over the entire domain, whereas the density changes from 67 kg m^{-3} on the oxygen side to 4 kg m^{-3} on the hydrogen side, with a minimum of 2 kg m^{-3} in the flame zone. The transport properties of Pr and $Sc(k)$ vary moderately around their mean values in the flame zone. In Fig. 8, oxygen is injected at a subcritical temperature of 100 K, but hydrogen remains in a supercritical state. The fluid compressibility factor undergoes a rapid variation from $Z \approx 0.18$ to 1.0 on the oxygen side when the local temperature increases across the critical point. The same phenomenon is observed for other thermodynamic and transport properties due to the abnormal changes near the critical point of oxygen. In spite of such steep changes of fluid properties in the low-temperature region on the oxygen side, the oxygen heats up rapidly and behaves like a perfect gas before entering the flame zone. The flame thickness

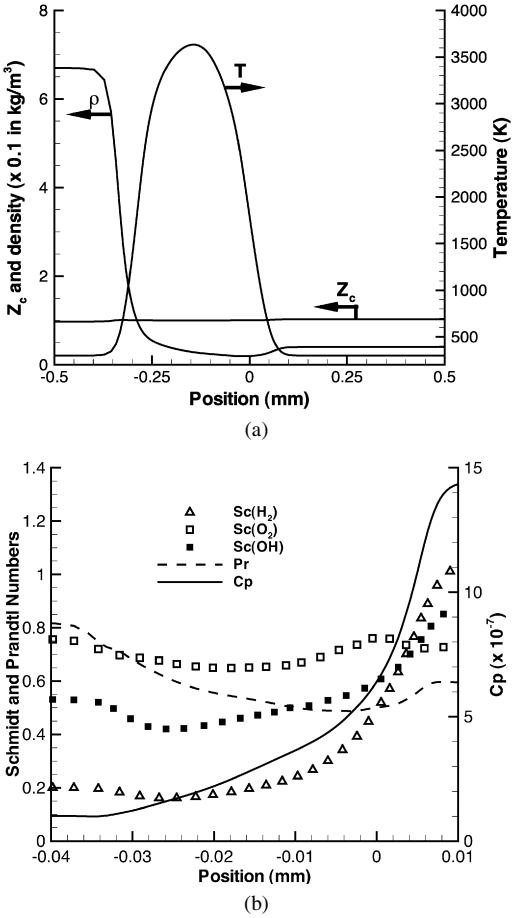

Fig. 7. Distributions of thermodynamic and transport properties for H_2/O_2 flame. $T_{O_2} = 300$ K, $T_{H_2} = 300$ K, $\epsilon_s = 2000\ s^{-1}$, and $p = 50$ bar.

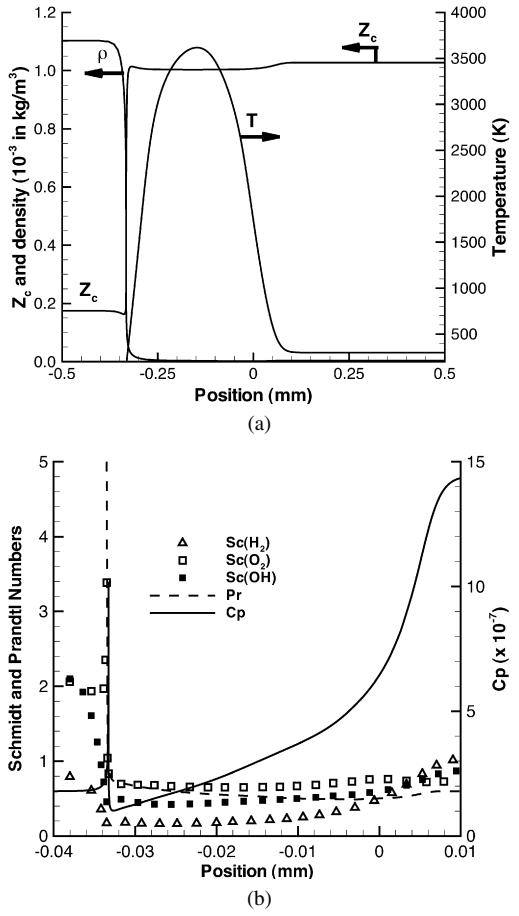

Fig. 8. Distributions of thermodynamic and transport properties for H_2/O_2 flame. $T_{O_2} = 100$ K, $T_{H_2} = 300$ K, $\epsilon_s = 2000\ s^{-1}$, and $p = 50.4$ bar.

as measured by the temperature profile thus becomes almost identical in Figs. 7 and 8 for $T_{O_2} = 100$ and 300 K, respectively. The influence of the oxygen inlet temperature and associated real-fluid effect in determining the flame behavior appear to be limited. The transport parameters (ρD or λ/C_p) are basically independent of pressure over most of the flowfield and have values close to those of their ideal-gas counterparts.

Fig. 9 shows the temperature distributions for four different pressures in the range 25–200 bar. The strain rate is fixed at 2000 s^{-1}, and two different oxygen inlet temperatures of $T_{O_2} = 300$ and 100 K are considered. At a given strain rate, an increase in pressure leads to a thinner flame with a higher flame temperature. A decrease in the oxygen inlet temperature from 300 to 100 K causes only a slight decrease of 20 K in the flame temperature. The ensuing enlargement of the flame is also quite moderate. This behavior can be further explored by considering the heat release rate

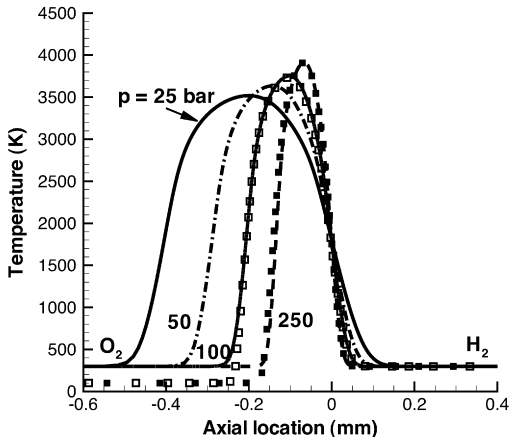

Fig. 9. Temperature profiles for H_2/O_2 counterflow diffusion flames at different pressures. $\epsilon_s = 2000\ s^{-1}$. $T_{H_2} = 300$ K and $T_{O_2} = 300$ K (lines) or 100 K (symbols).

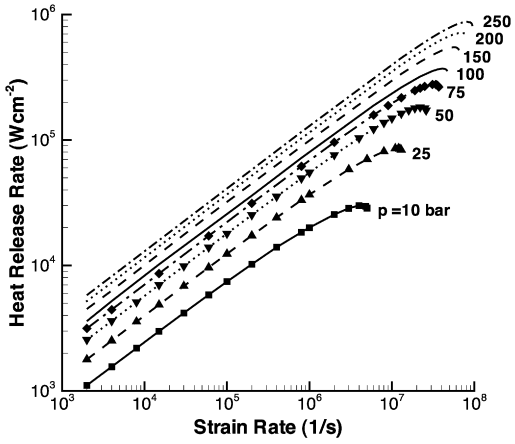

(a)

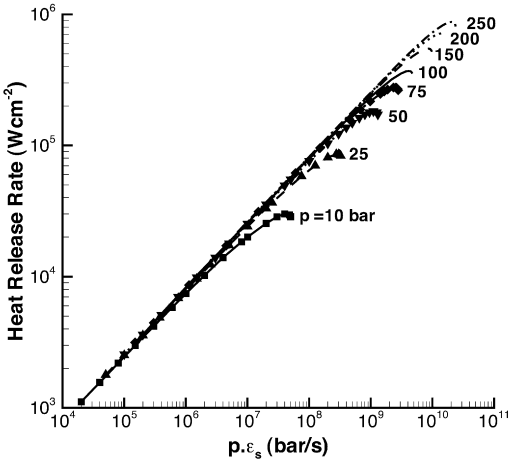

(b)

Fig. 10. Heat release rate per unit area as a function of (a) strain rate and (b) $p \cdot \epsilon_s$ for H_2/O_2 counterflow diffusion flames at different pressures. $T_{H_2} = 300$ K and $T_{O_2} = 300$ K.

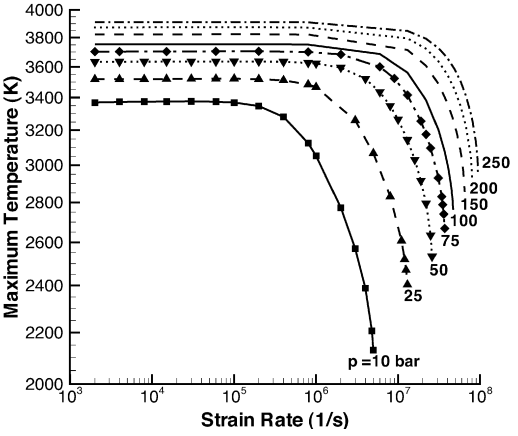

Fig. 11. Effect of strain rate on maximum temperature for H_2/O_2 counterflow diffusion flames at $T_{H_2} = 300$ K and $T_{O_2} = 300$ K for different pressures.

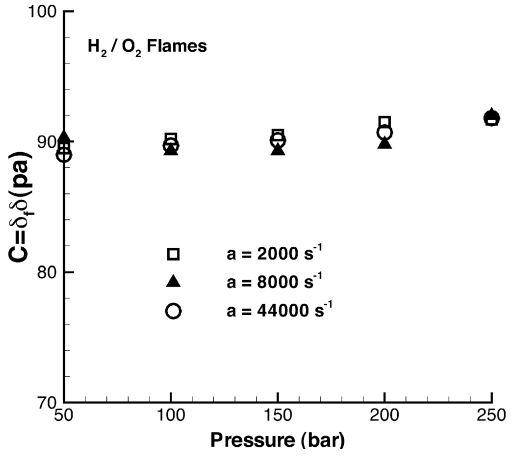

Fig. 12. Counterflow diffusion flame thickness parameter ($C = \delta_f\sqrt{p\epsilon_s}$) as a function of pressure for three different strain rates.

per unit flame area, $\dot{q}_s$.

$$\dot{q}_s = \int_{-\infty}^{+\infty} \left(\sum_{k=1}^{N_s} \bar{h}_k W_k \dot{\omega}_k \right) dy. \tag{24}$$

Fig. 10a shows the heat release rate as a function of the strain rate for the pressure range 10–250 bar. Both the oxygen and hydrogen inlet temperatures are set to 300 K. For a given pressure, the heat release rate $\dot{q}_s$ first increases linearly with the strain rate, reaches its maximum, and decreases slightly before extinction. The linear dependence of $\dot{q}_s$ with respect to the square root of the strain rate appears to be insensitive to pressure, although a higher pressure increases the strain rate and temperature at the extinction limit. The overall result can be correlated with the product of pressure and strain rate, $p\epsilon_s$. Fig. 10b shows the functional relationship of $\dot{q}_s \sim \sqrt{p\epsilon_s}$.

Fig. 11 shows the maximum temperature (T_{max}) as a function of strain rate. At low strain rates, T_{max} remains nearly constant. At higher strain rates, T_{max} decreases progressively to reach its quenching temperature. The extinction strain rate, ϵ_s^{ext}, which corresponds to the end point of each temperature profile in Fig. 11, is approximately proportional to the pressure and evolves with this parameter in a quasi-linear manner. Fig. 12 shows the flame thickness (δ_f) in the pressure range 50–250 bar for three different strain rates. Like at the subcritical pressures shown in Fig. 4, the result is plotted as a function of the C parameter, defined as $C = \delta_f\sqrt{p\epsilon_s}$. This parameter is nearly constant for the supercritical pressures considered herein.

4. Conclusion

A comprehensive analysis of laminar counterflow diffusion flames has been developed for general fluids. The model incorporates fundamental thermodynamics and transport theories, and can be applied to the entire regime of fluid thermodynamic states. In addition, cross-diffusion terms such as the Soret and Dufour effects are included for light species. As a specific example, undiluted H_2/O_2 flames have been studied over a broad range of pressures at both subcritical and supercritical conditions. The effects of pressure, strain rate, and oxygen inlet temperature on the flame behavior and energy-release rate were examined systematically. Results not only enhance the fundamental understanding of the flame properties under various flow conditions and fluid states, but also can be used as a submodel in the treatment of nonpremixed turbulent combustion. The calculated flame thickness δ_f and heat-release rate per unit flame area $\dot{q}_s$ were found to depend on the pressure p and strain rate ϵ_s through the correlations of $\delta_f \sim 1/\sqrt{p\epsilon_s}$ and $\dot{q}_s \sim \sqrt{p\epsilon_s}$, respectively. The extinction limit of the strain rate evolves with pressure in a quasi-linear manner. Significant real-fluid effects take place and manifest themselves by rapid property variations in the transcritical regime. The resultant influence on the flame properties, however, is limited, since the fluid behaves as a perfect gas when entering the high-temperature flame region. For H_2/O_2 mixtures, the impact of the Soret and Dufour effects appear to be insignificant at elevated pressures due to enhanced chemical reaction rates that override changes in diffusion. The Soret effect may still exert a nonnegligible influence on the extinction strain rate, as the present formulation of thermal diffusion does not cover the supercritical state. This issue requires further investigation.

Acknowledgments

This work was partly sponsored by the Air Force Office of Scientific Research under Grant FA 9550-04-1-0014, and partly sponsored by NASA through a Constellation University Institutes Project (CUIP) Grant. The authors gratefully acknowledge the support and advice given by Mitat Birkan, Claudia Meyer, Jeff Rybak, and Kevin Tucker.

References

[1] N. Darabiha, V. Giovangigli, S. Candel, M.D. Smooke, Combust. Sci. Technol. 60 (1988) 267–285.
[2] N. Darabiha, Combust. Sci. Technol. 86 (1992) 163–181.
[3] H.G. Im, C.K. Law, J.S. Kim, F.A. Williams, Combust. Flame 100 (1995) 21–30.
[4] V. Yang, Proc. Combust. Inst. 28 (2000) 925–942.
[5] C.J. Sung, J.B. Liu, C.K. Law, Combust. Flame 102 (1995) 481–492.
[6] T.M. Brown, M.A. Tanoff, R.J. Osborne, R.W. Pitz, M.D. Smooke, Combust. Sci. Technol. 129 (1997) 71–88.
[7] G. Balakrishnan, M.D. Smooke, F.A. Williams, Combust. Flame 102 (1995) 329–340.
[8] B.A. Williams, Combust. Flame 124 (2001) 330–333.
[9] R. Ben Dakhlia, V. Giovangigli, D.E. Rosner, Combust. Theory Model. 6 (2002) 1–17.
[10] M. Juniper, N. Darabiha, S. Candel, Combust. Flame 135 (2003) 87–96.
[11] T. Niioka, S. Hasegawa, T. Tsukamoto, J. Sato, Combust. Flame 86 (1991) 171–178.
[12] D. Schlotz, E. Gutheil, Combust. Sci. Technol. 158 (2000) 195–210.
[13] S. Candel, M. Juniper, G. Singla, P. Scouflaire, C. Rolon, Combust. Sci. Technol. 178 (2006) 161–192.
[14] M. Juniper, A. Tripathi, P. Scouflaire, J.-C. Rolon, S. Candel, Proc. Combust. Inst. 28 (2000) 1103–1109.
[15] W. Mayer, A. Schik, B. Vielle, C. Chauveau, I. Gokalp, D. Talley, R. Woodward, J. Propuls. Power 14 (1998) 835–842.
[16] G. Singla, P. Scouflaire, J.-C. Rolon, S. Candel, Proc. Combust. Inst. 30 (2005) 2921–2928.
[17] G. Singla, P. Scouflaire, J.-C. Rolon, S. Candel, Combust. Flame 144 (2006) 151–169.
[18] J.C. Oefelein, V. Yang, J. Propuls. Power 14 (1998) 843–857.
[19] J.C. Oefelein, Combust. Sci. Technol. 178 (2006) 229–252.
[20] N. Zong, V. Yang, Proc. Combust. Inst. 31 (2007) 2309–2317.
[21] J. Bellan, Prog. Energy Combust. Sci. 26 (2000) 329–366.
[22] N. Zong, H. Meng, S.Y. Hsieh, V. Yang, Phys. Fluids 16 (12) (2004) 4248–4261.
[23] S. Palle, C. Nolan, R.S. Miller, Phys. Fluids 17 (2005) 103601.
[24] C.H. Sohn, S.H. Chung, S.R. Lee, J.S. Kim, Combust. Flame 115 (1998) 299–312.
[25] H. Meng, V. Yang, J. Comput. Phys. 189 (2003) 277–304.
[26] R.J. Kee, G. Dixon-Lewis, J. Warnatz, M. Coltrin, J.A. Miller, A FORTRAN computer code package for the evaluation of gas phase multicomponent transport properties, Technical Report SAND86-8286 UC401, Sandia National Laboratories, 1986.
[27] M.D. Smooke, I.K. Puri, K. Seshadri, Proc. Combust. Inst. 21 (1986) 1783–1792.
[28] A. Ern, V. Giovangigli, Combust. Sci. Technol. 149 (1999) 157–181.
[29] G. Soave, Chem. Eng. Sci. 27 (1972) 1197.
[30] M.S. Graboski, T.E. Daubert, Ind. Eng. Chem. Process Des. Dev. 17 (1978) 443–450.
[31] B.E. Poling, J.M. Prausnitz, J.P. O'Connell, The Properties of Gases and Liquids, fifth ed., McGraw–Hill Int., Singapore, 2001.

[32] T.H. Chung, M. Ajlan, L.L. Lee, K.E. Starling, Ind. Chem. Eng. Res. 27 (1988) 671–679.
[33] A. Congiunti, C. Bruno, E. Giacomazzi, Supercritical combustion properties, AIAA Paper No. 2003-0478, 2003.
[34] S. Takahashi, J. Chem. Eng. Jpn. 7 (1974) 417.
[35] J. Li, Z. Zhao, A. Kazakov, F.L. Dryer, Int. J. Chem. Kinet. 36 (2004) 566–575.
[36] M.A. Muller, T.J. Kim, R.A. Yetter, F.L. Dryer, Int. J. Chem. Kinet. 31 (1998) 113–125.
[37] C.G. Fotache, C.J. Sung, C.J. Sun, C.K. Law, Combust. Flame 112 (1998) 457–471.
[38] A.M. Briones, S.K. Aggarwal, Int. J. Hydrogen Energy 30 (2005) 327–339.
[39] R.J. Kee, F.M. Rupley, J.A. Miller, Chemkin II: A FORTRAN chemical kinetics package for analysis of gas phase chemical kinetics, Technical Report SAND89-8009B, Sandia National Laboratories, 1993.
[40] J.A. Miller, R.E. Mitchell, M. Smooke, R.J. Kee, Proc. Combust. Inst. 19 (1982) 181–196.
[41] V.R. Katta, W.M. Roquemore, AIAA J. 36 (1998) 2044–2054.
[42] I. Glassman, Combustion, third ed., Academic Press, San Diego, 1996.
[43] C.K. Law, Combust. Sci. Technol. 178 (2006) 335–360.
[44] T. Daguse, T. Croonenbroek, J.-C. Rolon, N. Darabiha, A. Soufiani, Combust. Flame 106 (1996) 271–287.
[45] K. Harstad, J. Bellan, Int. J. Multiphase Flow 26 (2000) 1675–1706.
[46] D.E. Rosner, M. Arias-Zugasti, AIChE J. 53 (2007) 1879–1890.
[47] A. Ern, V. Giovangigli, Combust. Theory Model. 2 (1998) 349–372.
[48] R.G. Schmitt, P.B. Butler, N.B. French, Chemkin real gas: A FORTRAN package for analysis of thermodynamics properties and chemical kinetics in non-ideal systems, Chemkin Real Gas User's Guide, University of Iowa, 1993.